The Human Touch: Measuring Contact with Real Human Soft Tissues

DINESH K. PAI, University of British Columbia and Vital Mechanics Research, Canada
AUSTIN ROTHWELL, PEARSON WYDER-HODGE, and ALISTAIR WICK, University of British Columbia
YE FAN and EGOR LARIONOV, University of British Columbia and Vital Mechanics Research
DARCY HARRISON, Vital Mechanics Research
DEBANGA RAJ NEOG and COLE SHING, University of British Columbia

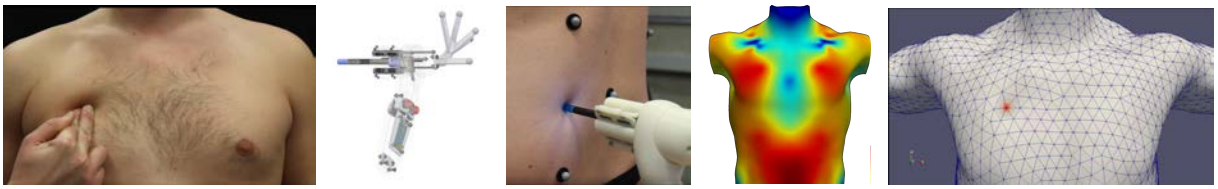

(a) (b) (c) (d) (e)

Fig. 1. The paper describes a complete pipeline for modeling contact with the human body (a). We developed a novel hand-held skin probe (b), incorporating a high resolution force/torque sensor and three cameras. The probe measures tissue properties at different locations on the body (c), while both probe and body are tracked by a Vicon motion capture system. The data are used to map the properties of our "sliding thick skin" tissue model over the participants body (d). Our data can be used to produce more realistic simulations of the human body in contact (e).

Simulating how the human body deforms in contact with external objects, tight clothing, or other humans is of central importance to many fields. Despite great advances in numerical methods, the material properties required to accurately simulate the body of a real human have been sorely lacking. Here we show that mechanical properties of the human body can be directly measured using a novel hand-held device. We describe a complete pipeline for measurement, modeling, parameter estimation, and simulation using the finite element method. We introduce a phenomenological model (the sliding thick skin model) that is effective for both simulation and parameter estimation. Our data also provide new insights into how the human body actually behaves. The methods described here can be used to create personalized models of an individual human or of a population. Consequently, our methods have many potential applications in computer animation, product design, e-commerce, and medicine.

CCS Concepts: • **Computing methodologies** → **Physical simulation**;

Additional Key Words and Phrases: human simulation, contact, measurement, soft tissues, finite element, biomechanics

Authors' addresses: Dinesh K. Pai, pai@cs.ubc.ca, University of British Columbia, Computer Science, Vancouver, BC, Vital Mechanics Research, Vancouver, BC, Canada; Austin Rothwell, acroth@cs.ubc.ca; Pearson Wyder-Hodge, p.wyderhodge@alumni.ubc.ca; Alistair Wick, alistair.wk@gmail.com, University of British Columbia, Vancouver, BC; Ye Fan, yefan@vitalmechanics.com; Egor Larionov, egor.larionov@gmail.com, University of British Columbia, Computer Science, Vancouver, BC, Vital Mechanics Research, Vancouver, BC; Darcy Harrison, darcy.harrison@vitalmechanics.com, Vital Mechanics Research, Vancouver, BC; Debanga Raj Neog, debanga@cs.ubc.ca; Cole Shing, coleshin@cs.ubc.ca, University of British Columbia, Computer Science, Vancouver, BC.

0730-0301/2018/8-ART58 $15.00
https://doi.org/10.1145/3197517.3201296

ACM Reference Format:
Dinesh K. Pai, Austin Rothwell, Pearson Wyder-Hodge, Alistair Wick, Ye Fan, Egor Larionov, Darcy Harrison, Debanga Raj Neog, and Cole Shing. 2018. The Human Touch: Measuring Contact with Real Human Soft Tissues. *ACM Trans. Graph.* 37, 4, Article 58 (August 2018), 12 pages. https://doi.org/10.1145/3197517.3201296

1 INTRODUCTION

Simulating the human body is one of the greatest challenges in computer graphics, and also in myriad fields of human endeavor ranging from industrial design to medicine.

Most human models used in computer graphics are purely kinematic, and cannot simulate how the body would react to internal and external forces. There have been significant recent advances in physics-based models of the human body, but these have focused on the numerical methods required for simulating soft tissues; the constitutive properties of these tissues have been chosen almost arbitrarily. Even though such simulations are very useful for producing physically plausible jiggles and bulges, their utility outside the entertainment industry has been limited.

By contrast, applications in product design, e-commerce, and medicine need trustworthy models, whose predictions can be relied upon to make decisions. For example, before you buy a tight-fitting pair of jeans or a sports bra online, a trustworthy simulation should predict how well it fits you, taking into account how your body will deform when the garment is worn. Such accurate and personalized human body simulations are out of reach today.

Why is this? Despite intense research effort, the human body remains one of the most mysterious and complex objects known to science. Soft tissues are composites made of many different living materials whose properties can vary significantly over the body, across individuals, and even under voluntary control (e.g., by flexing a muscle). It is not currently possible to simply look up the mechanical properties of, say, your shoulder and plug it into a simulation.

Despite these difficulties, our goal is to make such trustworthy simulations of the real behavior of the human body possible.

This goal immediately implies that it is no longer sufficient to have good simulation algorithms; we must measure the real behavior of the human body, and we must use these measurements to estimate the parameters of the model for each individual. Such data may also be aggregated to derive the distribution of these body parameters across a population.

There has been significant progress in the last decade in measuring human body *appearance and shape*, thanks to advances in computer vision and other optical scanning technologies. However, the spatial distribution of the *mechanical properties* needed for contact simulation cannot be easily measured by existing techniques. The mechanical behavior of soft tissues is highly non-linear; it is difficult to extrapolate properties derived from, say, passive videos or ultrasound elastography, to those that can represent soft tissue compression due to a garment or wearable device.

In this paper we show how contact properties of the human body can be directly measured using a novel hand-held device. Parameters required for an FEM simulation can be estimated from this data, and used for simulating personalized models of an individual. Our work complements the recent advances in numerical methods for soft tissue simulation by providing data-driven parameter values for more realistic simulations. In addition to enabling new applications for human simulation, analysis of these measurements provides new insights into how the human body actually behaves.

Our contributions are as follows. We developed the first system for *in vivo* measurement of spatially varying mechanical properties needed for simulating contact with the human body. We developed a complete pipeline for measuring and modeling contact properties of soft tissues. This includes a novel skin contact probe for rapid assessment of local contact properties of the skin. We propose a simple and effective "Sliding Thick Skin" (STS) model, and provide new data on the effective thickness of skin over the body. The entire system is easy to use with human participants from the general public, and enables large scale measurement and modeling of the real mechanical properties of living humans.

1.1 Related Work

We are not aware of any other work that has acquired the *distribution* of the mechanical properties of contact with the human body. However, due to the central importance of the human body to many different fields, there is an enormous literature that could relate to some aspects of our work. We can only briefly sketch the outlines of this literature here.

There is a long history, beginning with the arts, in measuring the *shape* of the human body. These methods, known as anthropometry, are widely used in the fields of ergonomics and industrial design, following the seminal work of Henry Dreyfuss [1967]. Dreyfuss created normative models of human body shape, called Joe and Josephine, to inform industrial design. More recent work includes the Jack animation system [Badler 1997], and the work of Body Labs (recently acquired by Amazon).

Human characters are central to computer animation, with a vast literature on kinematic methods for character animation. Here we will focus on the work most relevant to physically based human simulation using finite element methods (see [Sifakis and Barbič 2015] for a recent tutorial on the relevant numerical methods). One major focus has been to model and simulate muscles, with the hope of producing more realistic body shapes and skin movement for characters. See [Lee et al. 2010] for a recent survey focused on muscles. There have been increasingly detailed models that include musculoskeletal anatomy in a physically based simulation framework [Fan et al. 2014; Lee et al. 2009; Si et al. 2014; Sueda et al. 2008; Teran et al. 2005a] and to transfer the anatomy [Ali-Hamadi et al. 2013; Kadleček et al. 2016]. These methods are already used in both the movies and medicine, including the award winning Tissue system from Weta Digital; recent software includes Anatoscope, Vital Skin, and Ziva VFX. Many of these use musculoskeletal geometry and body shape derived from scans, but focus on simulation to obtain plausible results only. With few exceptions they did not measure properties of tissue deformation.

Some recent work estimated tissue properties without contact, relying on the excitation of the tissue dynamics by the subject's own motion. Sifakis et al. [2005] estimated tissue properties of the human face from the motion of dense motion capture markers attached to the face. Subsequently, there has been an explosion of recent work on markerless facial motion capture. Recently, Pons-Moll et al. [2015] estimated the parameters of a modal model using a 3dMD high resolution markerless motion capture system. Wang et al. [2015] estimated parameters of a co-rotated linear elasticity model of various soft objects measured using Kinect sensors. Kim et al. [2017], also estimated parameters of a co-rotated linear elasticity model, using the 3dMD data of Pons-Moll et al. [2015]. They used an FEM layer over a kinematically driven skinned inner shape, but in contrast to our work, they do not allow this layer to slide along the inner body layer. While such non-contact measurement is attractive for its simplicity, it is not suitable for modeling how soft tissues behave due to contact, since the tissues do not undergo sufficient compression. Moreover, the linear material models used in the above work are poorly suited for modeling tissues under large compression [Smith et al. 2017].

Very few papers have addressed estimating soft tissue properties under contact. Our work is inspired by the UBC Active Measurement Facility, which automatically captured a deformable object's shape, elasticity, and surface friction [Pai et al. 2001]. We propose a similar general approach, but now focused on measuring the properties of human skin and subcutaenous soft tissues. Kry and Pai [2006] measured contact force and displacement of the human hand during grasping and manipulation. However, they used this information to estimate the effective compliance of the joints and not of the soft tissues of the hand. Bickel et al. [2009] used a better, non-linear, soft tissue model in a similar fashion but used a simple force sensing resistor attached to a screwdriver to measure contact forces. Miguel et al. [2016] along with other recent work has estimated properties of cloth and other hyperelastic material which can be applied to soft tissues as well.

Layered soft tissue models of human skin have been used in surgical simulation (e.g., [Koch et al. 1996; Mitchell et al. 2016], but the tissue properties of skin have not been directly measured. There is also a large literature in biomechanics and dermatology on modeling

skin. Many state-of-the-art constitutive models are reviewed by Limbert [2017]. Some models are purely phenomenological, considering the skin as a homogeneous material described by a single relationship between strain and stress. Others consider the structure and geometric configuration of the micro-structural elements of the skin. Maurel et al. [1998] describe the critical features that a physically based skin model must consider: non-homogeneity, anisotropy, nonlinearity viscoelasticity, multiple layers/components. Flynn [2014] provides a detailed survey of state of the art structural models specifically for the dermis. Among phenomenological models, Lanir and Fung [1974] conclude, based on experiments with rabbit skin, that skin is rubber-like. This has led to the widespread adaptation to skin of the hyperelastic models of Rivlin and others, originally designed for rubber-like materials [Ogden 1972; Rivlin and Saunders 1951]. We use similar constitutive models in our paper.

2 A FRAMEWORK FOR MODELING HUMAN SOFT TISSUES

Here we briefly outline our measurement and modeling pipeline, and the rationale for our approach. The main steps are model selection, measurement, estimation, and simulation. The key constraint is that we are measuring *contact behavior* over *large areas* of the human body, *in vivo*. This eliminates the standard methods of placing a small tissue sample in a testing machine and applying carefully controlled loads or displacements, and requires us to make the measurement comfortable and easy from the point of view of the human participant or subject[1].

2.1 Models

Recent soft tissue models are based on the detailed structure of biological materials [Limbert 2017]. Our model is constrained by both the data and the applications. The applications we are targeting require efficient simulation of macroscopic contact behavior, such as the behavior of clothing on the body. On the other hand, the challenges of measuring humans in a non-clinical setting limits the data that can be acquired. There is little benefit from including myriad details of the ultrastructure of the soft tissues, such as thickness and composition of each of the layers, if we have no realistic hope of measuring the distribution of these details over the body.

Therefore we chose simpler phenomenological models that can be directly related to measurements, an approach that is sometimes known as "reality-based" modeling [Pai 2000]. Our model consists of a *body template* and *spatially varying constitutive properties*.

Our body template consists of an "inner body" surface covered with a layer of soft tissues bounded externally by a skin. Our focus is on the deformation of this soft tissue layer due to contact. We assume that the inner body motion is externally specified and imposes Dirchlet boundary conditions on the inner side of the soft tissue layer. For example, to produce different simulations, the inner body could be deformed using a kinematic animation rig or with a musculoskeletal simulation. The soft-tissue thickness is an essential spatially varying parameter that has a strong influence on the behavior of highly non-linear soft tissues.

[1]We will use the term *participant* to refer to person whose body was measured in this paper, since our methods apply in a general setting outside the laboratory.

Our pipeline can accommodate different constitutive model structures, since at present there is no clear consensus over what models are best for human tissues. Our focus is on estimating the parameters of the model from measurements. We assume that elastic behavior can be described by a hyperelastic model that can represent the nonlinear deformation behavior. We believe in Occam's razor, and favor using relatively simple models with as few parameters as possible, as long as they capture the significant features of our data. We propose a simple sliding thick skin material model (described below).

2.2 Measurement

We measure tissue deformation using a custom made hand-held probe (Sec. 3), equipped with a six-axis force sensor and a calibrated trinocular vision system. The probe and markers on the participant's body are tracked using a motion capture system (Vicon MX). In our main study we sampled each participant's skin at 15 locations on the torso. At each location the skin was probed four times, in different directions. Additional studies acquired data at a higher spatial resolution over selected regions and under different body conditions (e.g., muscles flexed or relaxed).

2.3 Estimation

The next step is to estimate model parameters from individual human participant data, which is essentially a process of large-scale data fitting and parameter interpolation. Estimating material models is extremely challenging; for example, [Ogden et al. 2004] remark "the fitting of experimental data within the framework of the mechanics (or thermomechanics) of elastomeric solids is a very delicate question," especially as the number of parameters grow.

Since the skin is relatively thin in many regions, with significant sliding behavior in the tangential direction, we propose and use the Sliding Thick Skin (STS) model. This models the observed orthotropy by representing soft tissue as a volumetric "thick skin" layer that can slide over the inner body surface. The volumetric part is modeled as non-linear isotropic hyperelastic material (a generalized Rivlin-type polynomial model). The inner surface of the thick skin is elastically coupled to the inner body surface upon which it slides. We estimate the material properties of the body at each probe location by fitting the output of the FEM simulation of a cylindrical tissue disk centered at the contact (a "skin puck") to the measured force and skin optical flow data. The probe's motion supplies Dirichlet boundary conditions at the point of contact. We search for parameter values that best fit the measured force and skin surface displacements. Similar procedures have been used in previous work (e.g., [Bickel et al. 2009; Pai et al. 2001] for parameter estimation.

2.4 Simulation

After estimating skin thickness and effective constitutive properties over the body, the body template is fitted to individual participants using body scans or marker data. The inner body shape is reconstructed from the fitted outer body shape and the volume between the two is discretized into a tetrahedral mesh. We use scattered data interpolation to generalize the sparse measurements for soft

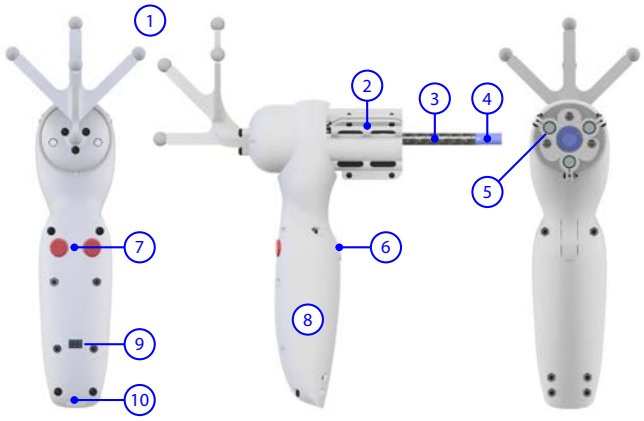

Fig. 2. The Skin Probe. 1: 3D tracking marker arrangement on the "tentacle"; 2: Single-piece probe "head", holding the cameras and force sensor; 3: Carbon fiber composite probe stem; 4: Quick-change, magnetic-lock probe tip; 5: Front-facing cameras; 6: Front trigger button; 7: Rear input buttons; 8: Ergonomic handle, housing Arduino micro-controller; 9: Externally accessible Arduino ISP header (reprogramming port); 10: Exit point for probe cables, with internal strain relief clamp.

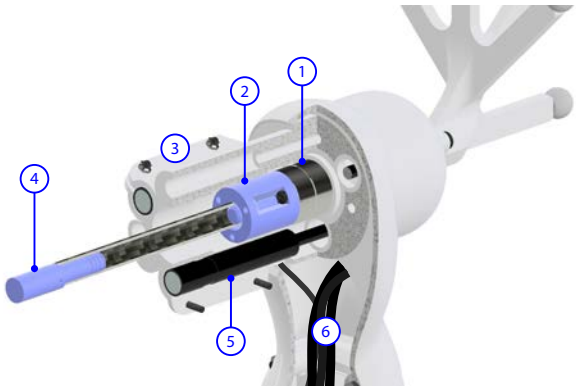

Fig. 3. Cutaway view of the the probe's sensor "head" section. 1: Embedded force/torque sensor; 2: SLA-printed probe stem mount, which secures the stem to the force sensor; 3: Integrated clamps hold the probe camera at an adjustable distance from the tip; 4: The probe tip, showing the internal channel housing the locking magnets, and pinhole used for securing tips expecting negative loadings; 5: Endoscope camera; 6: Camera and force sensor cable routing to probe base

tissue properties to estimate the distribution of these properties throughout the body. Any non-linear finite element method for nearly incompressible hyperelastic material may now be used to simulate the behavior of the body (akin to [Gast and Schroeder 2014; McAdams et al. 2011; Sifakis and Barbic 2012; Teran et al. 2005b]). Our implementation has some specific features that make it well suited for simulating our data driven models. We simulate the volumetric thick skin layer sliding over the inner body surface, as described above. This requires a very smooth sliding surface which we represent as an implicit surface modeled using Hermite radial basis functions (HRBF) [Macêdo et al. 2009; Vaillant et al. 2013; Wendland 2005]. These steps result in a personalized body shape and soft tissue model for an individual participant which can be used for simulating contact with deformation. We demonstrate the utility of such models with some examples.

3 DESIGN AND FABRICATION OF SKIN PROBE

3.1 Design

The handheld probe we use for our data collection (Fig. 2) is a custom in-house design, specifically tailored for the project and produced with rapid prototyping techniques. The bulk of the design work was carried out in 3D solid CAD software (Inventor 2017, Autodesk, California USA).

The probe houses three miniature high-definition RGB cameras (USB Endoscope, Abask, Taiwan), a six-axis force/torque sensor (F/T Nano 17, ATI Industrial Automation, North Carolina USA), three user input buttons, and a micro-controller board (Arduino LLC, Turin Italy). The experimenter receives visual feedback during operation through a user interface (UI) on a separate monitor. This UI is directly controllable using the buttons on the probe.

The cameras are placed to provide a clear view of the skin patch around the probing point, with overlapping fields-of-view that eliminate all occlusions around the probe except at the point of contact. The design also enables future stereoscopic 3D analysis of the patch's deformation.

We briefly sketch our design process. The design underwent rapid iterative changes throughout the project. An initial prototyping phase with non-functional sample parts resulted in general decisions on the overall shape of the probe, including the pistol-grip design – which optimizes grip angle for the probing locations under consideration – and rear placement of the marker tracking assembly, which keeps the assembly out of the way of both the probe cameras and experimenter. After this initial prototyping phase, the device saw five major iterations, with a general trend of increasing size and additional features.

The final probe is optimized for ergonomics, durability over multiple experiments, and ease of use. This includes use by a solo experimenter; the probe's input buttons allow an individual to perform initial calibration, then select and create recorded "trials" with no other experimenters present. This was desirable as it improved participant privacy and comfort, and left project members free for data processing tasks. With this in mind, and drawing inspiration from video-game console controllers, the probe buttons are laid out for easy operation with one hand. Two buttons are placed for operation with the user's thumb, on the probe's back – that is, facing the experimenter. The third button is integrated into a "trigger" on the rear of the probe, operated with a forefinger. In addition, the probe's large, organically-shaped handle is designed to be held comfortably with a one or two-handed grip.

With a sensitive force sensor mounted back from the cameras (Fig. 3), a relatively long shaft was required to reach the probing point. This had to be lightweight, to minimize the shaft mass' influence on the sensor; compact, to avoid occluding the camera's views of the skin patch; and extremely stiff, to ensure a rigid transformation

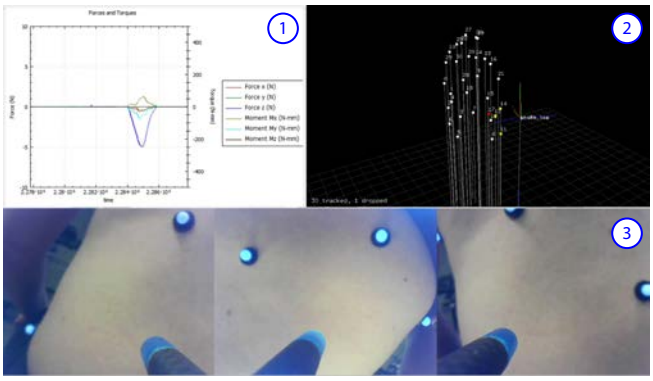

Fig. 4. The probe capture software. 1: Live feed of the forces and torques applied to the probe tip, showing a recent touch; 2: Visualizer window, displaying the real-time positions of the participant markers and the skin probe tip through a user-adjustable virtual camera; 3: Live split view from the three probe cameras, showing the probe shaft and tip in-frame, along with the participant and several markers.

between the probing location and the probe itself, even as forces are applied to the tip. After experimenting with metal shafts and tubes, we switched to a lightweight carbon-fiber tube, with a custom-made 3D-printed mounting and a magnetically-locking, quick-change tip.

In any application where experiment hardware is in direct contact with members of the public, safety is even more of a concern than usual. While contact forces in our application are low, we have taken care to avoid sharp edges and exposed electronics in the probe design, to minimize risk of injury to both the experimenters and participants.

3.2 Fabrication

The probe was fabricated with a combination of 3D printing technologies. We used a Fused-Deposition Modeling (FDM) printer (Dimension 1200es, Stratasys, Minnesota USA) to build the larger parts of the probe, such as the handle and marker tracking assembly. These were made out of ABS plastic, a fairly typical thermoplastic frequently used for injection-molded parts of consumer products. ABS FDM results in semi-elastic parts which stretch rather than break, and which are approximately 75% as strong as their injection-molded equivalents. Parts in the tip assembly, which slot directly together, required finer tolerances than those which could be achieved through FDM printing, so we opted for stereolithographic resin printing (SLA), using a Form 2 printer (Formlabs, Massachusetts USA). The only significant structural element which is not 3D printed is the carbon fiber stem, a hollow tube which was hand-cut to length.

3.3 Capture Software

The Skin Probe software (Fig. 4) serves primarily to monitor data streams from the various sensors and Vicon system, and to consolidate these streams into recordings sampled at up to 120Hz. It also allows the experimenter to execute automated optical flow post-processing on the captured video feeds. The software is controlled through a graphical user interface written in C++, and using the Qt 5 application library. An additional 3D view of the capture volume is provided through our visualizer application, which was written in Python and can display both live and recorded data from the main application. Another important role of the SkinProbe software is to calibrate the Skin Probe before experiments: details of this process are discussed in Sec. 4.3.

We use Vicon Blade to monitor the Vicon system. Blade captures the position in 3D space of any detected markers in the capture volume, and provides robust tracking of the transformations of rigid "props" like the Skin Probe and calibration board. Blade relays this capture data via a streaming API to the main Skin Probe application, where we implemented our own predictive marker tracking solution for the less-rigid bodies of our test participants.

Our software stack was necessarily developed in sync with the probe, with the same iterative design philosophy. Features like serial communication with the probe's on-board micro-controller were added as-needed to support additions to the probe. Outside of the main application, we developed support software for calibration (see section 3.4.1) and data post-processing tasks. The accompanying video demonstrates the probe and the software in action.

Our probe design, software, and experiment protocols are now thoroughly proven through dozens of pilot studies and live data capture sessions. The handheld nature of the device lets us quickly and easily take multiple measurements in a single short session, the tracked markers on both the probe and the participant allow us to precisely locate these measurements on the participant's body, letting us map the participant's tissue in a novel and compelling way. The probe's extensible design also leaves several interesting opportunities for future work.

3.4 Estimating Optical Flow

The probe's trinocular camera system (Figs. 2, 3) generates a three-component video feed, from which we estimate optical flow vector fields used to analyze the surface motion of participant's skin. Here we briefly describe our camera calibration and flow estimation processes.

3.4.1 Calibration. We simultaneously calibrate all cameras post-assembly using a custom calibration pattern (shown in the accompanying video), with three checkerboard sub-patterns of differing width matched up to the three cameras. During the calibration pass, camera images containing the checkerboards are identified and analyzed using standard OpenCV camera calibration functions to estimate the corresponding camera's intrinsic and extrinsic parameters. Using a combination of multiple checkerboards, we can estimate 2D transformation matrices $\mathcal{M}_{ij}$, representing the relative affine transformations between the views of the i^{th} and j^{th} cameras. These are later used to transform and align the calculated optical flows into a reference image coordinate frame. The exact choice of reference frame is arbitrary: we simply use the local frame of the 1^{st} camera. We also record a user-defined mask for each camera, used to exclude the probe shaft and tip from flow calculations. Alongside the consistent reference frame, this masking allows us to align and stitch the individual views to generate a *composite* view, a single image encompassing the skin region surrounding the probe contact point.

3.4.2 Optical Flow Computation. After each skin probe experiment, we estimate optical flows resulting from skin movements in each camera view, using the Dense Inverse Search (DIS) optical flow algorithm [Kroeger et al. 2016]. Since our cameras are calibrated, we can transform simulated flows computed from an FEM simulation of skin deformation into each camera's image space, to compare the predictions of a simulation with estimated optical flows. With runtime performance in mind, we used a GPU implementation of the DIS flow algorithm available in OpenCV contribution module [Bradski 2000]. There are three implementations available – medium, fast, and ultrafast – each distinguished by their respective runtime performance, and each carrying an inverse tradeoff in average endpoint error (EPE). We opted for the 'medium' implementation, which allowed us to run batched flow post-processing in minutes rather than hours, while still achieving high quality optical flow.

4 MEASURING HUMAN SOFT TISSUES

We have developed and refined a complete measurement pipeline that addresses the important constraints of *in vivo* mechanical measurement of human tissues. First, the measurements are taken by humans holding a small hand held device, and not an intimidating machine. This is important since the probe has to apply forces on the skin. The measurements are taken as the participant is standing, or while they are sat comfortably on a stool in a relaxed pose. Second, it is difficult for human participants to hold still. By tracking both the probe and the body, we compute the precise relative motion of the probe with respect to the body, even if the participant moves. Third, we need to measure over large portions of the body. With our system this can be done easily, since participant and probe can be repositioned almost freely. One major difficulty of contact measurement is that we need to measure tissue deformation close to the contact point. Unlike recent work on dense face and body motion capture [Klaudiny et al. 2017; Wu et al. 2016], we cannot use world-fixed cameras due to significant occlusion from the probe. This problem is mitigated in our project by the probe's integrated cameras, which capture these occluded areas in their overlapping fields-of-view (Sec. 3.1). Another difficulty is that the experimenter has to be close to the participant and probe, and can block the motion capture markers. We minimized this difficulty by careful placement of the cameras (Fig. 5) and also by designing a "tentacle" to hold the probe markers in a relatively unobstructed manner (Fig.2). Finally, the measurement process is very quick, requiring less than 5 seconds per touch, and 30 minutes for data collection after initial setup. This is important to avoid participant fatigue and boredom.

We now briefly describe our measurement process.

4.1 Motion Capture

To record the position and orientation of the skin probe and the skin patches being probed on the participant, an 8-camera Vicon MX motion-capture system, recording at 120 fps, is used. Captured data are synchronized with force measurements and streamed for real-time display and further processing, and saved to disk (Sec. 3.3). To prevent marker occlusion caused by the experimenter obtaining measurements, the density of Vicon cameras is higher toward the opposite side of where the experimenter stands (see Fig. 5). This allows us to focus use of the available cameras in areas the markers are not occluded.

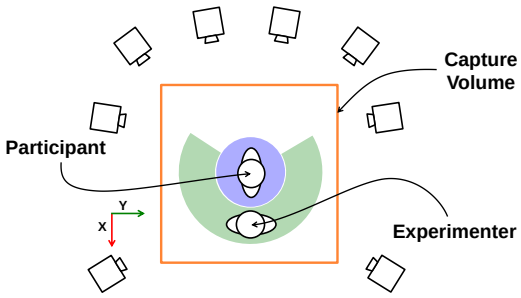

Fig. 5. Capture volume surrounded by eight Vicon MX cameras. Note the higher density of Vicon cameras at the far side of the room to reduce occlusion caused by the experimenter when probing. The green area shows the zone where the experimenter records data from, the blue area shows where the participant is situated.

4.2 Marker and Probing Locations

Retro-reflective markers are attached to the skin using medical-grade adhesive tape. Experimenters place the markers in pre-defined locations, using palpation and a human body diagram to locate the positions. Marker locations are sex-specific; 30 markers are attached to males and 36 markers are attached to females (see Fig. 6). Markers are placed such that each probing location has at least three markers nearby and the marker positions roughly define the participant's body shape.

On both males and females, 15 locations on the arms and torso were probed (see Fig. 6). In one participant we densely sampled the shoulder (23 locations) and waist (27 locations) on one side (see inset figure). These probing locations are pre-defined and located in a similar manner to the marker positions. The probing locations are marked on the participant's skin with a washable pen, to ensure accuracy of the probing. Note that the actual locations that were probed at each touch are known precisely since we track the probe tip with the motion capture system. The probing locations were chosen to ensure local consistency of underlying tissue (e.g., no probing locations are on the border of muscle and bone), and to highlight the variability of human tissue across the torso. For example, locations were chosen on the bony regions on the clavicle, muscular regions on the pectoralis major, and fatty regions on the lower abdomen.

4.3 Probe Calibration

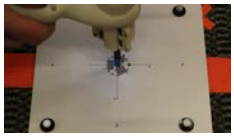

The probe is calibrated prior to each measurement session, in three steps. First, we estimate the transformation between the probe's reference frame and the probe tip by placing the probe's tip on the center of our tracked calibration board. Next, we stabilize the force sensor readings (which have an intrinsic non-zero "bias") by taring the readings at two orientations: one with the shaft pointing down, to

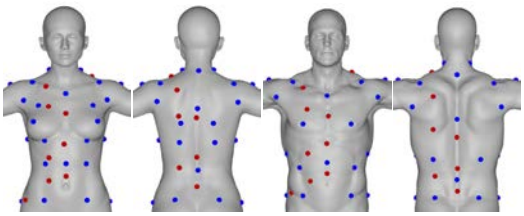

Fig. 6. Marker and probe locations on Females (left) and Males (right). Blue locations are where retro-reflective markers are placed. Red locations are where the probe is touched to the tissue and data is collected

yield zero lateral forces and zero torques; and one with the shaft held out horizontally, to yield zero axial force.

The shaft, while lightweight, still has a measurable mass which we wish to eliminate from our readings. We obtain several samples of orientation and force/torque data by moving the probe through various (arbitrary) orientations, with no external loading (see video). From these we estimate the mass and center of mass of the probe shaft, which can subsequently be used to correct the force readings in any orientation.

With these calibrations, the combined force and torque (called a "wrench" in mechanics) can be transformed from the sensor frame to the probe tip to accurately report the actual contact wrench applied to the body (Fig. 7). This is done using the 6×6 transpose of the Adjoint matrix of the coordinate transformation. Please see, for example, the textbook by Murray et al. [1994], Chapter 2, Section 5, for background on wrenches and their transformations.

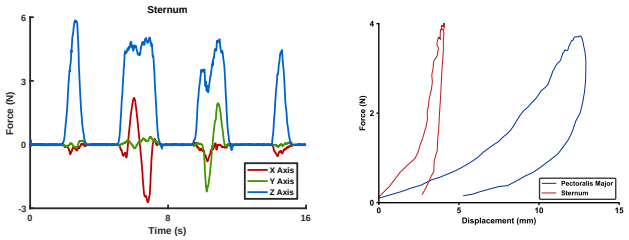

Fig. 7. Raw data captured after probe calibration. Recorded forces showing four probe contacts (left) and recorded tip position while probing the sternum and the pectoralis major muscle (right). Note the hysterisis as the probe returns to the initial contact location.

4.4 Participants and Protocol

Measurement and recruiting protocols were approved by UBC's Research Ethics Board. To date, we have measured a wide range of participants (14 participants, 7 female, three ethnicities; ages 22-59 years, heights 159-189 cm, and weight 44-93 kg). All provided written informed consent. In future work, we will greatly expand the number of participants. The goal of this paper is to describe the measurement and modeling technology that will be used in these future studies.

In the capture volume, the probe tip is touched to the skin of the participant in the 15 pre-specified probing locations (see Fig. 6). By assuming symmetry we can use each measurement a second time to estimate properties of the contralateral side, effectively doubling the number of locations. This is not an essential part of our protocol and was only done to reduce time and avoid fatigue. For each location, three different probing actions are performed to achieve various deformations of the skin and highlight the anisotropic properties of the underlying tissue. One probe was in the direction of the skin normal (conducted twice per probing location), and two were roughly side-to-side contacts in orthogonal directions (see inset and supplementary video). Importantly, the probe tip maintains contact with the skin throughout the whole touch; medical grade adhesive tape is placed on the probe tip to reduce slippage. In addition, experimenters aim to make contact with the skin such that the probe shaft is perpendicular to the skin of the probing location. Real-time feedback is given to the experimenter to ensure that 3-5 Newtons of force is applied to each probing location on the participant's body.

5 ESTIMATION

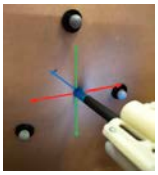

Most work in biomechanics has focused on estimating constitutive properties of soft tissue samples removed from the body. However, such data are not useful on their own for simulating entire humans. Tissue behavior due to external contact is profoundly affected by the boundary conditions imposed by the deep layers of the body, which are largely unknown. Moreover, since soft tissues are highly non-linear in compression, the thickness of the tissue layer has great influence on the observed surface tractions due to contact.

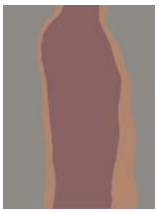

Therefore we need to generalize material property estimation to recover the *effective thickness* of the soft tissue layer at the same time. The inset figure shows the saggital section of the body with the innerbody surface estimated from measurements of a subject. Note that effective thickness may not correspond to an actual thickness of a part of body, since we are measuring the homogenized effect of many layers of tissues with complex boundaries. Rather, it is a thickness that, when used with a corresponding constitutive property, best approximates the deformation behavior at the surface. In addition, human soft tissues are relatively thin in many regions, with significant sliding behavior in the tangential direction. The underlying biomechanical reason for this is that the connective tissue binding the dermis to subcutaneous muscles and bone has to be somewhat loose in many areas to avoid impeding movement.

We propose to model the specific features of this observed orthotropy by representing the soft tissue covering the body as a volumetric thick skin layer that can slide over the inner body surface. This "Sliding Thick Skin" (STS) model is in contrast to the "thin skin" model proposed by Li et al. [2013], which does not model the deformation in the direction normal to the skin surface. The volumetric part is modeled as a non-linear isotropic hyperelastic material (a generalized Rivlin-type polynomial model) [Ogden 1972; Rivlin and Saunders 1951]. The inner surface of the thick skin is

elastically coupled to the inner body surface upon which it slides, approximating both the effect of connective tissue fascia and neighbouring soft tissues. At each probe location we estimate the classical material parameters of the thick skin volume, and also its thickness and the stiffness of coupling to the inner body. Even though our parameters are inspired by biomechanical structures, we emphasize that it is a phenomenological model. For instance, the "thickness" must not be interpreted as the actual thickness of skin (however that is defined) but an effective value that can be used for simulation.

5.1 Constitutive Model

The mathematical model describing STS material can be written as follows. Let $\boldsymbol{x}$ denote the set of vertices of a tetrahedral FEM mesh, and $\underline{\boldsymbol{x}} \subset \boldsymbol{x}$ be the vertices on the inner aspect of the mesh. The inner body is represented as a smooth implicit surface. We use Hermite radial basis functions (HRBF) to represent the inner body, with centers offset from the outer surface of the body by the estimated thickness. The HRBFs define a scalar field $c(\boldsymbol{x})$ whose zero level set defines the inner body surface. We constrain the inner vertices $\underline{\boldsymbol{x}}$ to slide along the implict surface. For a quasistatic simulation we solve the following constrained optimization problem:

$$\boldsymbol{x} = \underset{\boldsymbol{x}}{\operatorname{argmin}} \, (W_e(\boldsymbol{x}) + W_s(\underline{\boldsymbol{x}})), \tag{1}$$

$$s.t. \quad c(\underline{\boldsymbol{x}}) = c(\underline{\boldsymbol{x}}_0). \tag{2}$$

Here W_e and W_s are the energies for elasticity and coupling potential. $\underline{\boldsymbol{x}}_0$ represents the rest configuration of the inner vertices $\underline{\boldsymbol{x}}$. The sliding constraint $c(\underline{\boldsymbol{x}}) = c(\underline{\boldsymbol{x}}_0)$ may take non-zero value on the right hand size. This allows us to have an inner body surface that's not conforming to the zero level set. This approach has the benefit that we can discretize the full human body once and cull tets that are entirely in the inner body, and constrain the vertices on the remaining boundary to sliding on level sets of the inner body. This avoids constant remeshing as estimated thickness varies across participants.

The elastic energy W_e used in our STS model is based on the classical compressible neo-Hookean model with a few extra terms taken from the generalized Rivlin model (also known as polynomial hyperelastic model). More specifically,

$$W_e = \frac{\mu}{2}(\mathrm{tr}(\boldsymbol{C}-\boldsymbol{I}) - 2\log(\det(\boldsymbol{F}))) + \frac{\mu_4}{8}\,\mathrm{tr}((\boldsymbol{C}-\boldsymbol{I})^4) + \frac{\lambda}{2}\log^2(\det(\boldsymbol{F})), \tag{3}$$

The quartic term helps capture the biphasic nature of the observed force-displacement relationship.

The coupling potential W_s controls sliding resistance of the tissue. It's currently modeled as zero length spring, but W_s can be general elastic like potential. In our implementation, we used a simple linear spring since we observed that the tangential forces are well approximated by a linear model in the range of forces we used (see Fig. 9).

$$W_s = \frac{\kappa}{2}(\underline{\boldsymbol{x}} - \underline{\boldsymbol{x}}_0)^T(\underline{\boldsymbol{x}} - \underline{\boldsymbol{x}}_0). \tag{4}$$

5.2 Estimating Material Properties and Thickness

To estimate the material properties of the human body at each contact location, the behavior of a 3D FEM simulation can be fit to the measured force and optical flow. We call the 3D model used for estimation "skin puck" due to its shape and propensity to slide. Our model assumed that the skin probe maintained contact with the skin throughout the whole touch, without any slippage from the initial contact location; this is ensured during measurements by using a small patch of double sided medical tape on the probe tip. Based on that assumption, Dirichlet boundary conditions are applied at the contact locations, and drive the simulation of the puck.

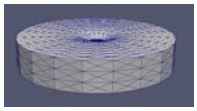

By minimizing the difference between simulated force and recorded force, and between simulated optical flow and recorded optical flow, the material properties of the tissue can be estimated. We took a derivative free approach for optimizing material properties, and treat the simulation as a black box. This allows us to use off-the-self optimization solvers. For our STS model, material properties to be optimized are stiffness, thickness, volume resistance and coupling strength. Whenever thickness is changed, we remesh the skin puck based on the current thickness estimate, and keep the ratio between thickness and radius a constant. The constant is chosen to be small enough that probing deformation can be considered local. The initial guess for thickness is provided as the maximum indentation plus a few millimeters.

Estimation for each skin puck at different measurement locations are done independently in parallel. Once all estimations finish we interpolate these point estimates to the rest of the mesh using scattered data interpolation. This data interpolation was done by solving bi-harmonic equations with Dirichlet boundary conditions. Boundary values are chosen by averaging point estimates.

The next step is to build an inner body based on spatially varying thickness. As mentioned in Sec. 5.1, the inner body is represented using a HRBF surface. We sampled a sufficient number of HRBF sites from the surface of the body mesh, and moved these sites along surface normal direction inwards by the thickness sampled on the surface mesh. This set of new HRBF sites defines the inner body, which the STS model can slide on.

5.2.1 Force. Following probe calibration (see Sec. 3.3), forces recorded from the force/torque sensor inside the probe are transformed to the probe tip coordinate frame, allowing the recorded forces to be compared against the forces that arise from the point of contact in the 3D FEM tissue simulation. The difference between recorded and simulation force is used as the error metric for optimization. The force optimization objective is given by $\sum_{i=1}^{n} ||\boldsymbol{f}_r^i - \boldsymbol{f}_p^i||_2$, where $\boldsymbol{f}_r$ is the recorded force, $\boldsymbol{f}_p$ is the force predicted by the simulation, and n is the number of samples used from the touch location. We used around 10 force samples for estimation.

One challenge we encountered during estimation is skin hysteresis, where the force displacement curve is different during the loading and the unloading phases (see Fig. 7). For fitting the parameters to the proposed material model, we use the data from loading phase only.

5.2.2 Optical Flow. Optical flow estimated from the camera images is compared to the tissue simulation by transforming the 3D skin puck from simulation space to camera image coordinates using the projection matrices estimated from the optical flow calibration

(see Sec. 3.4). Once the skin puck vertices are transformed to camera coordinates, optical flow of the simulation can be computed at identical pixel coordinates as the optical flow estimated from the recorded camera images. Here the masks recorded during camera calibration are useful, as we are only interested in the motion of the real and simulated tissue. The masks are applied to the simulation and recorded optical flow to remove data that are sampled from areas of the image where the skin is blocked by the probe shaft. For each skin contact, we minimize the optical flow error between the flow estimates from each camera and the predictions of the model, summed over the recorded frames for the touch.

6 RESULTS

One of the most direct and useful results from our study is the ability to estimate the distribution of effective thickness of our STS model over the body. See Fig. 8. The map agrees qualitatively with our expectations but provides quantitative values that can be used in a simulation.

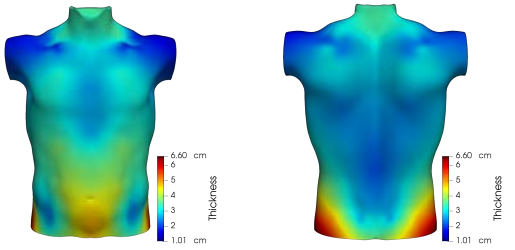

Fig. 8. Thickness map for a male subject, shown on template, front (left) and back (right) views. The body was coarsely sampled at 15 locations and finely sampled at 50 more locations around the hip and shoulder areas. These samples were interpolated to other parts of the torso. The thickness varies from about 1mm (over the bony regions, such as over the clavicle and vertebrae) to over 6cm (abdomen).

We estimated material parameters that minimized the force error. Figure 9 depicts the force-displacement data and model predictions at two nearby locations on the chest. We note that even though the two locations are a few centimeters apart, they have dramatically different force responses. The model fits the data reasonably well, especially over softer regions of the body. Figure 10 shows the same data as a function of time during indentation of the probe.

Next, we examined how well the estimates generalize from one location to another nearby, anatomically similar, location. We compared two locations at the crest of the shoulder on the trapezius muscle. See Fig. 11.

With our measurement pipeline, we can estimate and store material maps on the body, for subsequent simulation. Fig. 12 depicts the material parameters estimated from one subject.

A key feature of our sliding thick skin model is the ability simulate more realistic tissue movement under tangential loads. The accompanying video shows the simulation that reconstructs the probing experiment. Figure 13 shows the difference between simulating skin with our sliding thick skin model and without tissue sliding.

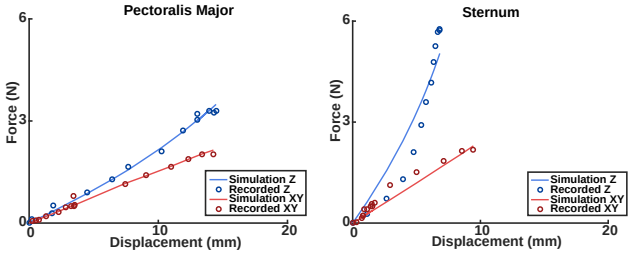

Fig. 9. Estimated model and fit at two nearby locations on the chest of a male subject, on the breast (left) and on the sternum (right). Our model captures the different stiffness at the two locations. The sternum area has a thin layer of skin over the breastbone, while the pectoral area is softer due to muscle and fat. Notice that the tangential forces are nearly linear in displacement in the typical range of displacements.

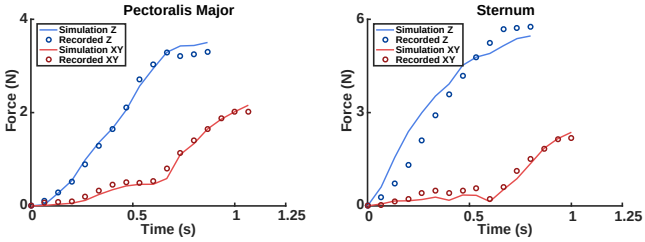

Fig. 10. Simulated and measured force from a touch in which the probe was first moved into the skin and then moved tangentially, at the same locations as in Fig. 9.

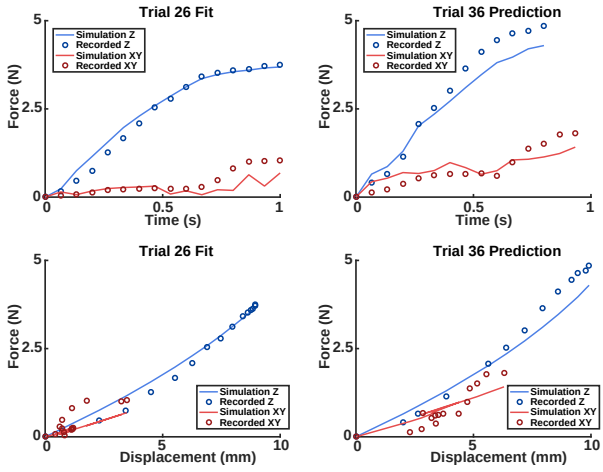

Fig. 11. Generalization of tissue properties. Model parameters were estimated from one location on the shoulder over the superior trapezius muscle (left plot, location 26), and used to predict the force response at a second location on the shoulder 2.5cm away (right plot, location 36). The top row shows the evolution of forces over time, and the bottow row shows the force-displacement curves. Note that the forces in the tangential (XY) directions are lower in the normal (Z) direction, and many data points are clustered near the origin of the plot. The response has good qualitative agreement, despite the fact that location 36 is closer to the neck and hence stiffer.

An example demonstrating how measured properties improve the realism of the simulation is a tight belt around the hip, where the

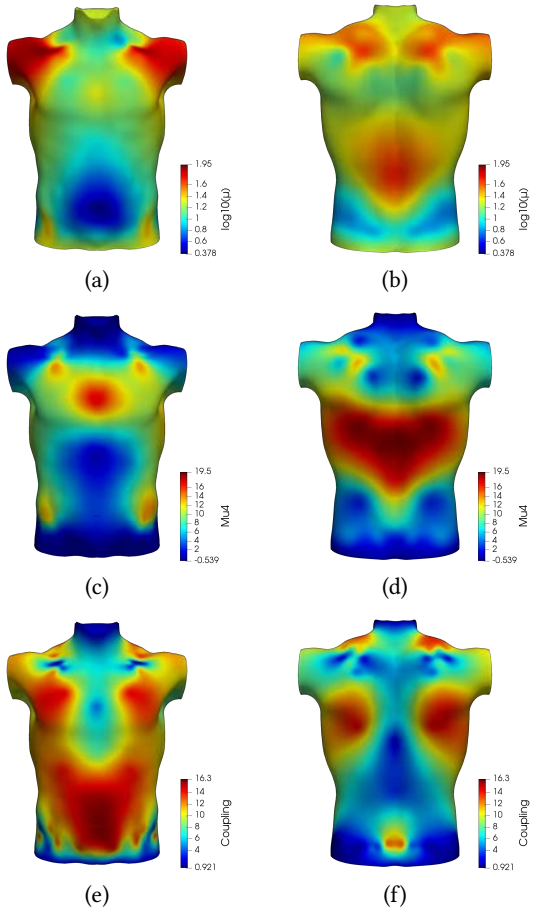

Fig. 12. Material maps for a male participant, shown on fitted body, front (left) and back (right) views. (a,b) show μ, the shear modulus, on a logarithmic scale for visualization. The front upper chest around the clavicle and shoulder are the stiffest. The abdomen, breast, and hip areas are the softest, even in a young male. The back appears to be more uniform, except for high stiffness around the vertebral column. (c,d) show μ_4 the coefficient of the quartic term. (e,f) depict the coupling stiffness with the inner body. Interestingly, we see that areas without much underlying muscle between skin and bone are the most loosely coupled.

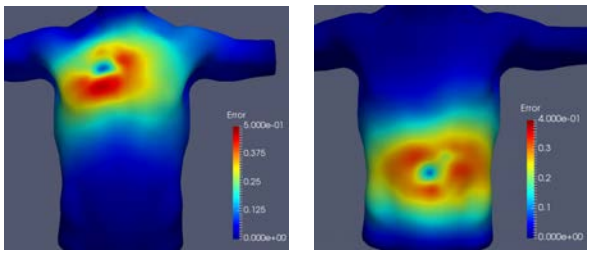

Fig. 13. Displacement error (in cm) between a simulation with sliding skin, and one in which soft tissue is fixed to inner body. We simulated the effects of a tangential touch on chest (left) and on the stomach (right).

abdomen meets the pelvic bone. To evaluate the effect of spatially varying thickness and material properties we simulated a belt in two ways. In one, we used constant skin thickness (corresponding to the abdomen) and averaged tissue properties. In another, we used our measured, spatially varying thickness and material properties. See Figure 14. The deformations are similar at the abdomen, as expected, but with measured properties we see more realistic deformation around the pelvic bone. Figure 15 visualizes the displacement magnitude in false color.

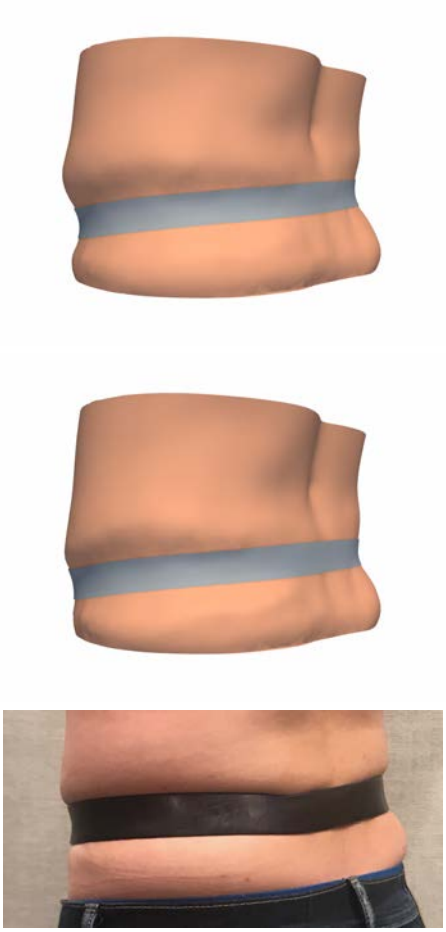

Fig. 14. A tight belt wrapped around the hip is simulated with constant thickness and material properties (top) and measured, spatially varying thickness and material properties (middle). The deformation appears to match the actual deformation of the participant better (bottom). The deformation is much more realistic near the pelvic bone (left contour), where there is little fat and muscle between skin and bone.

7 CONCLUSION

Measuring the properties of individual human bodies, *in vivo*, is extremely challenging but also essential for greater realism. In this paper we took the first steps to build a complete measurement pipeline to make these measurements possible. We addressed the

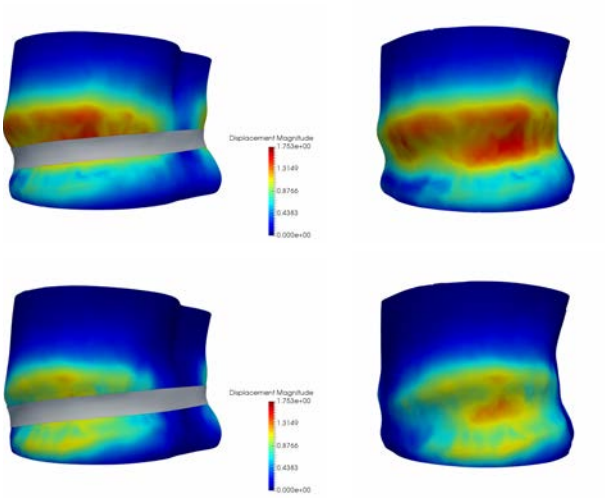

Fig. 15. Visualization of displacement. Using measured values we directly capture the effect of the underlying anatomy and tissue properties that reduce the deformation at the pelvic bone. **Left:** Magnitude of surface displacements, corresponding to the belt simulations shows in Fig. 14, with uniform properties (top) and our measured properties (bottom). Note that the displacement magnitude includes both indentation and motion along the tangent. **Right:** Different view of same data, along the medio-lateral axis of the body. The effect of the bony projection of the pelvic bone (anterior superior iliac spine, or ASIS) is clearly seen on the left of the image.

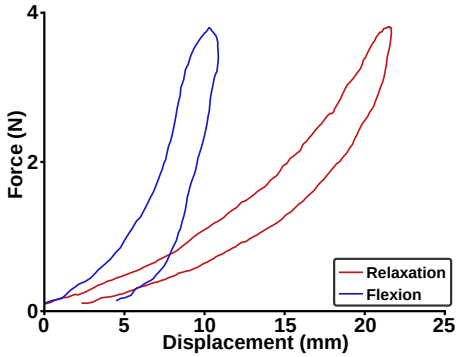

Fig. 16. Raw force – displacement curves measured from a location on a biceps muscle. In one condition, the biceps was relaxed; in the other, it was isometrically flexed in the same pose, by supporting a 6.8 kg weight in the hand. Note that the muscle is significantly stiffer when active.

main challenges by developing a fast and easy-to-use measurement system for mapping the tissue properties over the human body. The results to date are promising, and show that it is now possible to build detailed models of contact with an individual's body. Such models could open many new application areas in e-commerce, surgery, product design, and more realistic virtual humans.

There are several limitations that we hope to address in future work. We do not currently estimate skin friction. Skin friction does not follow a simple Coulomb friction model and depends significantly on hydration, which may need to be measured. Internal friction and energy dissipation within the soft tissues is not yet included in the model. While the material properties of skin and subcutaneous fat are relatively stable, muscles are stiffer when activated. See Figure 16. Modeling this dependence on muscle activation is a topic for future work, and may entail replacing the inner body with a musculoskeletal simulation (e.g., [Fan et al. 2014]). Wrinkling of skin is also not captured in our current model. Wrinkling requires a multi-layer tissue model to capture the physics of how wrinkles form. Recent work has shown that skin wrinkle formation can be explained by a stiff outer layer (corresponding to stratum corneum) and a softer basement layer. Wrinkles could be detected using multiview stereo from the trinocular vision system our probe. Our optical flow estimation method was less reliable than our force measurements, and could be improved, potentially with a different and more expensive choice of algorithm. We also currently do not utilize multiview stereo to estimate skin deformation in depth. Finally, we have not measured a sufficiently large number of participants to draw general conclusions about the distribution of material parameters over the human body. This mainly requires time and logistical resources to measure a large number of participants.

Despite the limitations, this paper described the first complete pipeline to quickly acquire and analyze touch data from human participants. With these novel data in hand, we can explore new, highly realistic, personalized models of the physical behavior of the human body.

ACKNOWLEDGMENTS

This work was funded by an NSERC Idea-to-Innovation grant and Vital Mechanics Research, Inc. Additional support was provided by ICICS, Canada Foundation for Innovation, NSERC Discovery grants, and the Canada Research Chairs Program.

REFERENCES

D. Ali-Hamadi, T. Liu, B. Gilles, L. Kavan, F. Faure, O. Palombi, and M.-P. Cani. 2013. Anatomy transfer. *ACM Transactions on Graphics (TOG)* 32, 6 (2013), 188.

N. Badler. 1997. Virtual humans for animation, ergonomics, and simulation. In *Nonrigid and Articulated Motion Workshop, 1997. Proceedings., IEEE.* IEEE, 28–36.

B. Bickel, M. Bächer, M. A. Otaduy, W. Matusik, H. Pfister, and M. Gross. 2009. Capture and modeling of non-linear heterogeneous soft tissue. *ACM Transactions on Graphics (TOG)* 28, 3 (2009), 89.

G. Bradski. 2000. The OpenCV Library: Dense Inverse Flow. https://docs.opencv.org/3.3.1/da/d06/classcv_1_1optflow_1_1DISOpticalFlow.html. *Dr. Dobb's Journal of Software Tools* (2000). Accessed: 2017-12-25.

H. Dreyfuss et al. 1967. Measure of Man. (1967).

Y. Fan, J. Litven, and D. K. Pai. 2014. Active volumetric musculoskeletal systems. *ACM Transactions on Graphics (TOG)* 33, 4 (2014), 152.

C. Flynn. 2014. Fiber Matrix Models of the Dermis. In *Computational Biophysics of the Skin.* CRC Press, 133–160.

T. F. Gast and C. Schroeder. 2014. Optimization Integrator for Large Time Steps. In *Proceedings of the ACM SIGGRAPH/Eurographics Symposium on Computer Animation (SCA '14).* Eurographics Association, Aire-la-Ville, Switzerland, Switzerland, 31–40. http://dl.acm.org/citation.cfm?id=2849517.2849523

P. Kadleček, A.-E. Ichim, T. Liu, J. Křivánek, and L. Kavan. 2016. Reconstructing personalized anatomical models for physics-based body animation. *ACM Transactions on Graphics (TOG)* 35, 6 (2016), 213.

M. Kim, G. Pons-Moll, S. Pujades, S. Bang, J. Kim, M. Black, and S.-H. Lee. 2017. Data-Driven Physics for Human Soft Tissue Animation. *ACM Transactions on Graphics, (Proc. SIGGRAPH)* 36, 4 (2017). http://dx.doi.org/10.1145/3072959.3073685

M. Klaudiny, S. McDonagh, D. Bradley, T. Beeler, and K. Mitchell. 2017. Real-Time Multi-View Facial Capture with Synthetic Training. *Computer Graphics Forum* 36, 2 (2017), 325–336. https://doi.org/10.1111/cgf.13129

R. M. Koch, M. H. Gross, F. R. Carls, D. F. von Büren, G. Fankhauser, and Y. I. Parish. 1996. Simulating facial surgery using finite element models. In *Proceedings of the 23rd annual conference on Computer graphics and interactive techniques*. ACM, 421–428.

T. Kroeger, R. Timofte, D. Dai, and L. Van Gool. 2016. Fast optical flow using dense inverse search. *European Conference on Computer Vision* (2016), 471–488.

P. G. Kry and D. K. Pai. 2006. Interaction capture and synthesis. *ACM Transactions on Graphics* 25, 3 (July 2006), 872–880.

Y. Lanir and Y. Fung. 1974. Two-dimensional mechanical properties of rabbit skin-II. Experimental results. *Journal of biomechanics* 7, 2 (1974), 171IN9175–174182.

D. Lee, M. Glueck, A. Khan, E. Fiume, and K. Jackson. 2010. A survey of modeling and simulation of skeletal muscle. *ACM Transactions on Graphics* 28, 4 (2010), 1–13.

S.-H. Lee, E. Sifakis, and D. Terzopoulos. 2009. Comprehensive biomechanical modeling and simulation of the upper body. *ACM Transactions on Graphics (TOG)* 28, 4 (2009), 99.

D. Li, S. Sueda, D. R. Neog, and D. K. Pai. 2013. Thin Skin Elastodynamics. *ACM Trans. Graph. (Proc. SIGGRAPH)* 32, 4 (July 2013), 49:1–49:9.

G. Limbert. 2017. Mathematical and computational modelling of skin biophysics: a review. In *Proc. R. Soc. A*, Vol. 473. The Royal Society, 20170257.

I. Macêdo, J. P. Gois, and L. Velho. 2009. Hermite Interpolation of Implicit Surfaces with Radial Basis Functions. In *2009 XXII Brazilian Symposium on Computer Graphics and Image Processing*. 1–8. https://doi.org/10.1109/SIBGRAPI.2009.11

W. Maurel, Y. Wu, N. M. Thalmann, and D. Thalmann. 1998. *Biomechanical models for soft tissue simulation*. Springer.

A. McAdams, Y. Zhu, A. Selle, M. Empey, R. Tamstorf, J. Teran, and E. Sifakis. 2011. Efficient Elasticity for Character Skinning with Contact and Collisions. In *ACM SIGGRAPH 2011 Papers (SIGGRAPH '11)*. ACM, New York, NY, USA, Article 37, 12 pages. https://doi.org/10.1145/1964921.1964932

E. Miguel, D. Miraut, and M. A. Otaduy. 2016. Modeling and Estimation of Energy-Based Hyperelastic Objects. In *Computer Graphics Forum*, Vol. 35. Wiley Online Library, 385–396.

N. M. Mitchell, T. W. King, A. Oliker, E. D. Sifakis, et al. 2016. A Real-Time Local Flaps Surgical Simulator Based on Advances in Computational Algorithms for Finite Element Models. *Plastic and reconstructive surgery* 137, 2 (2016), 445e–452e.

R. Murray, Z. Li, and S. S. Sastry. 1994. *A mathematical introduction to robotic manipulation*. CRC Press.

R. Ogden. 1972. Large deformation isotropic elasticity-on the correlation of theory and experiment for incompressible rubberlike solids. In *Proceedings of the Royal Society of London A: Mathematical, Physical and Engineering Sciences*, Vol. 326. The Royal Society, 565–584.

R. Ogden, G. Saccomandi, and I. Sgura. 2004. Fitting hyperelastic models to experimental data. *Computational Mechanics* 34, 6 (2004), 484–502.

D. K. Pai. 2000. Robotics in Reality-based Modeling. In Robotics Research*: the Ninth International Symposium*. Springer-Verlag, 353–358.

D. K. Pai, K. v. d. Doel, D. L. James, J. Lang, J. E. Lloyd, J. L. Richmond, and S. H. Yau. 2001. Scanning Physical Interaction Behavior of 3D Objects. In *Proceedings of the 28th Annual Conference on Computer Graphics and Interactive Techniques (SIGGRAPH '01)*. ACM, New York, NY, USA, 87–96. https://doi.org/10.1145/383259.383268

G. Pons-Moll, J. Romero, N. Mahmood, and M. J. Black. 2015. Dyna: A model of dynamic human shape in motion. *ACM Transactions on Graphics (TOG)* 34, 4 (2015), 120.

R. S. Rivlin and D. Saunders. 1951. Large elastic deformations of isotropic materials. VII. Experiments on the deformation of rubber. *Philosophical Transactions of the Royal Society of London A: Mathematical, Physical and Engineering Sciences* 243, 865 (1951), 251–288.

W. Si, S.-H. Lee, E. Sifakis, and D. Terzopoulos. 2014. Realistic biomechanical simulation and control of human swimming. *ACM Transactions on Graphics (TOG)* 34, 1 (2014), 10.

E. Sifakis and J. Barbic. 2012. FEM Simulation of 3D Deformable Solids: A Practitioner's Guide to Theory, Discretization and Model Reduction. In *ACM SIGGRAPH 2012 Courses (SIGGRAPH '12)*. ACM, New York, NY, USA, Article 20, 50 pages. https://doi.org/10.1145/2343483.2343501

E. Sifakis and J. Barbič. 2015. Finite Element Method Simulation of 3D Deformable Solids. *Synthesis Lectures on Visual Computing: Computer Graphics, Animation, Computational Photography, and Imaging* 1, 1 (2015), 1–69.

E. Sifakis, I. Neverov, and R. Fedkiw. 2005. Automatic determination of facial muscle activations from sparse motion capture marker data. In *Acm transactions on graphics (tog)*, Vol. 24. ACM, 417–425.

B. Smith, F. de Goes, and T. Kim. 2017. Stable Neo-Hookean Flesh Simulation. *ACM Trans. Graph.* (Dec. 2017).

S. Sueda, A. Kaufman, and D. K. Pai. 2008. Musculotendon Simulation for Hand Animation. *ACM Trans. Graph. (Proc. SIGGRAPH)* 27, 3 (2008), 83:1–83:8.

J. Teran, E. Sifakis, S. S. Blemker, V. Ng-Thow-Hing, C. Lau, and R. Fedkiw. 2005a. Creating and simulating skeletal muscle from the visible human data set. *IEEE Transactions on Visualization and Computer Graphics* 11, 3 (2005), 317–328.

J. Teran, E. Sifakis, G. Irving, and R. Fedkiw. 2005b. Robust Quasistatic Finite Elements and Flesh Simulation. In *Proceedings of the 2005 ACM SIGGRAPH/Eurographics Symposium on Computer Animation (SCA '05)*. ACM, New York, NY, USA, 181–190. https://doi.org/10.1145/1073368.1073394

R. Vaillant, L. Barthe, G. Guennebaud, M.-P. Cani, D. Rohmer, B. Wyvill, O. Gourmel, and M. Paulin. 2013. Implicit skinning: real-time skin deformation with contact modeling. *ACM Transactions on Graphics (TOG)* 32, 4 (2013), 125.

B. Wang, L. Wu, K. Yin, U. M. Ascher, L. Liu, and H. Huang. 2015. Deformation capture and modeling of soft objects. *ACM Trans. Graph.* 34, 4 (2015), 94–1.

H. Wendland. 2005. *Scattered Data Approximation: Cambridge Monographs on Applied and Computational Mathematics No. 17*. Cambridge University Press, GB, Chapter 16.2 - Hermite-Birkhoff interpolation.

C. Wu, D. Bradley, M. Gross, and T. Beeler. 2016. An Anatomically-constrained Local Deformation Model for Monocular Face Capture. *ACM Trans. Graph.* 35, 4, Article 115 (July 2016), 12 pages. https://doi.org/10.1145/2897824.2925882